

From steady to chaotic solutions in a differentially heated cavity of aspect ratio 8

Charles-Henri Bruneau^{*,†} and Mazen Saad

*Mathématiques Appliquées de Bordeaux, Université Bordeaux 1, 351 cours de la Libération,
33405 Talence, France*

SUMMARY

A splitting method is used for the temperature and the velocity–pressure unknowns to solve the time-dependent thermal convection problem in an 8:1 enclosure (International Journal for Numerical Methods, this issue). High performance is obtained by means of incomplete Cholesky conjugate gradient for the temperature equation on one hand and a multigrid procedure for Navier–Stokes equations on the other hand. The approximation is achieved by second- and third-order finite differences on staggered grids. The stability of the steady solution is analysed by the computation of the first Lyapunov exponent. The periodic flow at $Ra=3.4 \times 10^5$ is widely discussed and some investigations have been done for some higher Rayleigh numbers. Copyright © 2002 John Wiley & Sons, Ltd.

KEY WORDS: natural convection; multigrid method; linear stability; Lyapunov exponent

1. INTRODUCTION

It has become possible to compute solutions of complex flows in a differentially heated cavity, especially in two dimensions. By increasing the Rayleigh number it is thus quite easy to give a qualitative behaviour of the solutions from steady state to chaos. An important question is the accuracy of the computed solutions or in other words the quantitative meaning of these solutions.

In this paper, the determination of the critical Rayleigh number corresponding to the loss of stability of the steady solution to the benefit of a periodic solution is first achieved. There are at least two ways to verify the stability of a steady solution. The first one requires us to compute the eigenvalues or some eigenvalues of the matrix of the linearized problem in the neighbourhood of the steady solution. This is done successfully in References [1, 2] despite the huge amount of computation needed. The second approach used in this paper is rather direct, it consists in computing the first Lyapunov exponent by solving the linearized system. This corresponds to seeing asymptotically how a solution normalized at initial time goes to zero

*Correspondence to: C.-H. Bruneau, Mathématiques Appliquées de Bordeaux, Université Bordeaux 1, 351 cours de la Libération, 33405 Talence, France.

†E-mail: bruneau@math.u-bordeaux.fr

when the time goes to infinity. Lyapunov exponents are usually computed using a long-time direct simulation which can be achieved with the same code used for the direct simulation of the non-linear problem. The convergence is very fast for low Rayleigh numbers and becomes slower in the neighbourhood of the critical Rayleigh number. Just above the critical Rayleigh number a non-skew-symmetric periodic solution is captured.

In a second part, the behaviour of the periodic solution at $Ra=3.4 \times 10^5$ is investigated and quantitative data of various physical quantities are given on a set of grids. This value of the Rayleigh number was selected as a test case at the session computational predictability of natural convection flows in enclosures of the first MIT Conference on Computational Fluid and Solid Mechanics [3]. There is a large range of Rayleigh numbers around $Ra=3.4 \times 10^5$ for which the solution remains periodic. Then, the qualitative behaviour of some solutions at higher Rayleigh numbers are provided.

2. OUTLINE OF THE METHOD

2.1. Governing equations

The non-dimensional governing equations for the time-dependent thermal convection problem are the energy equation written in terms of temperature coupled to the Navier–Stokes equations for incompressible fluids. The full description of the physical problem is given in References [4, 5]. The differentially heated cavity problem is investigated in the 8:1 enclosure. That means that the height is 8 times larger than the width and that the vertical walls are maintained at a constant temperature in time. The non-dimensional governing equations in primitive variables are set in the 2D domain $\Omega=(0, W) \times (0, H)$ with aspect ratio $H/W=8$ and boundary $\partial\Omega=\Gamma_{\text{left}} \cup \Gamma_{\text{right}} \cup \Gamma_{\text{bottom}} \cup \Gamma_{\text{top}}$ as follow:

$$\begin{aligned} \partial_t U - \sqrt{\frac{Pr}{Ra}} \Delta U + \nabla p &= -U \cdot \nabla U + e_y \theta & \text{in } \Omega \times (0, T) \\ \nabla \cdot U &= 0 & \text{in } \Omega \times (0, T) \\ \partial_t \theta - \frac{1}{\sqrt{RaPr}} \Delta \theta &= -U \cdot \nabla \theta & \text{in } \Omega \times (0, T) \end{aligned} \quad (1)$$

where $U=(u, v)$, p and θ are the velocity, the pressure and the temperature, respectively, and e_y the unit vector in the vertical direction. The cavity is filled with fluid of Prandtl number Pr equal to 0.71 for air. The Rayleigh number is $Ra=g\beta\Delta TL^3/\nu\alpha$ with g the gravitational acceleration, β the coefficient of thermal expansion, ΔT the temperature difference between the hot and cold walls, ν the kinematic viscosity and α the thermal diffusivity. The Rayleigh number is the only parameter of the problem, and various regimes from steadiness to transition can be obtained by increasing this number.

These equations are associated to the initial conditions

$$U=U_0 \quad \text{and} \quad \theta=\theta_0 \quad \text{in } \Omega \quad (2)$$

and the boundary conditions

$$U=0 \quad \text{on } \partial\Omega \times (0, T)$$

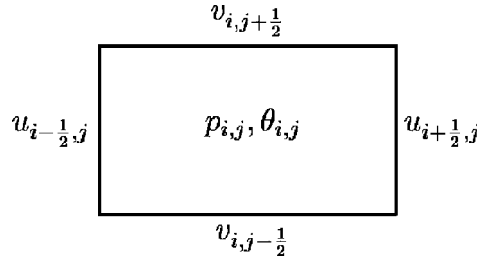


Figure 1. A staggered cell.

$$\begin{aligned} \theta = \frac{1}{2} \quad \text{on } \Gamma_{\text{left}} \times (0, T), \quad \theta = -\frac{1}{2} \quad \text{on } \Gamma_{\text{right}} \times (0, T) \\ \partial_y \theta = 0 \quad \text{on } \Gamma_{\text{bottom}} \cup \Gamma_{\text{top}} \times (0, T) \end{aligned} \tag{3}$$

2.2. Numerical approximation

The thermal convection problem is solved in temperature and velocity–pressure by a split-step in time: For θ^n and (U^n, p^n) given, θ^{n+1} is the solution of

$$\begin{aligned} \frac{\theta^{n+1} - \theta^n}{\delta t} - \frac{1}{\sqrt{RaPr}} \Delta \theta^{n+1} = -U^n \cdot \nabla \theta^n \quad \text{in } \Omega \\ \theta^{n+1} = \frac{1}{2} \quad \text{on } \Gamma_{\text{left}}, \quad \theta^{n+1} = -\frac{1}{2} \quad \text{on } \Gamma_{\text{right}} \\ \partial_y \theta^{n+1} = 0 \quad \text{on } \Gamma_{\text{bottom}} \cup \Gamma_{\text{top}} \end{aligned} \tag{4}$$

and (U^{n+1}, p^{n+1}) is the solution of

$$\begin{aligned} \frac{U^{n+1} - U^n}{\delta t} - \sqrt{\frac{Pr}{Ra}} \Delta U^{n+1} + \nabla p^{n+1} = -U^n \cdot \nabla U^n + e_y \theta^{n+1} \quad \text{in } \Omega \\ \nabla \cdot U^{n+1} = 0 \quad \text{in } \Omega \\ U^{n+1} = 0 \quad \text{on } \partial \Omega \end{aligned} \tag{5}$$

All the terms on the left-hand side of these equations are discretized by second-order centred finite differences. The unknowns are given on a staggered uniform grid, the temperature and the pressure are located at the centre of the cell, and the velocity components are located at the middle of the sides as shown in Figure 1. This implies that the divergence free condition is satisfied on each cell in the following sense:

$$(\nabla \cdot U)_{i,j} \approx \frac{u_{i+1/2,j} - u_{i-1/2,j}}{\delta x} + \frac{v_{i,j+1/2} - v_{i,j-1/2}}{\delta y}$$

Let us point out to the reader that due to the use of staggered grids the discretization of the diffusion terms at the boundary yields modified formulas as

$$(\partial_{xx} \theta)_{1,j} \approx (\frac{8}{3} \theta_{1/2,j} - 4 \theta_{1,j} + \frac{4}{3} \theta_{2,j}) / (\delta x)^2 \quad \text{with } \theta_{1/2,j} = \frac{1}{2} \quad \text{on } \Gamma_{\text{left}}$$

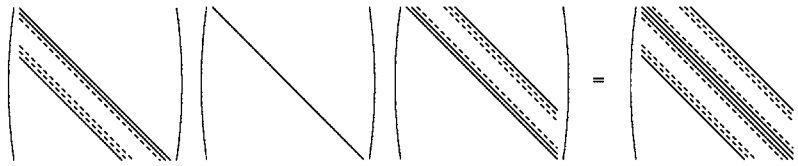


Figure 2. $L D' L$ Factorized matrix.

The advective terms which appear on the right-hand side of (4) are discretized by a third-order Murman scheme. Precisely, the term $u \partial_x \theta$ is approximated by

$$(u \partial_x \theta)_{i,j} \approx \begin{cases} \frac{1}{3} u_{i+1/2,j} \Delta_{i+1/2,j} \theta + \frac{5}{6} u_{i-1/2,j} \Delta_{i-1/2,j} \theta - \frac{1}{6} u_{i-3/2,j} \Delta_{i-3/2,j} \theta & \text{if } u_{i-1/2,j} > 0 \\ \frac{1}{3} u_{i-1/2,j} \Delta_{i-1/2,j} \theta + \frac{5}{6} u_{i+1/2,j} \Delta_{i+1/2,j} \theta - \frac{1}{6} u_{i+3/2,j} \Delta_{i+3/2,j} \theta & \text{if } u_{i+1/2,j} < 0 \end{cases}$$

where $\Delta_{i-1/2,j} \theta = (\theta_{i,j} - \theta_{i-1,j}) / \delta x$, and the term $v \partial_y \theta$ is discretized in the same way.

The convection terms in Equation (5) are also approximated by a third-order Murman scheme. For instance

$$(u \partial_x v)_{i,j-1/2} \approx \begin{cases} \frac{1}{3} u_{i+1/2,j-1/2} \Delta_{i+1/2,j-1/2} v + \frac{5}{6} u_{i-1/2,j-1/2} \\ \quad \times \Delta_{i-1/2,j-1/2} v - \frac{1}{6} u_{i-3/2,j-1/2} \Delta_{i-3/2,j-1/2} v & \text{if } u_{i-1/2,j-1/2} > 0 \\ \frac{1}{3} u_{i-1/2,j+1/2} \Delta_{i-1/2,j+1/2} v + \frac{5}{6} u_{i+1/2,j+1/2} \\ \quad \times \Delta_{i+1/2,j+1/2} v - \frac{1}{6} u_{i+3/2,j+1/2} \Delta_{i+3/2,j+1/2} v & \text{if } u_{i+1/2,j+1/2} < 0 \end{cases}$$

where $u_{i+1/2,j-1/2}$ is obtained by linear interpolation. The other terms are discretized in the same way.

The discrete solution of the thermal equation (4) is obtained by the incomplete Cholesky conjugate gradient method. The matrix of the linear system associated to problem (4) is a symmetric pentadiagonal matrix, but the incomplete Cholesky factorization is performed on an 11 diagonals matrix as shown in Figure 2. This factorization improves the efficiency of the incomplete Cholesky conjugate gradient on the original matrix by a factor 3.

While the Navier–Stokes equations are solved by means of a multigrid method with a cell-by-cell Gauss–Seidel relaxation smoother. The five unknowns for U and p of each cell are strongly coupled and solved simultaneously (see for instance [6, 7] for more details). As the temperature gradient is in the X -direction, we take a finer space-step in that direction than in the Y -direction. Namely on the domain $(0, 1) \times (0, 8)$ the coarsest grid is a 5×25 mesh. Then we build a sequence of grids by refining by two in each direction, so the second grid is a 10×50 mesh and so on. The computations are presented on fine grids up to 320×1600 (see Table I). The stopping criteria are based on the residuals that must be less than 10^{-6} and 10^{-5} , respectively, for Equations (4) and (5). No tricks of the trade are used to stabilize the computational process. But due to the explicit treatment of the non-linear terms a CFL condition is required.

Table I. Successive grids for the multigrid resolution.

Grids	Number of points	δx	δy
1	5×25	0.2	0.32
2	10×50	0.1	0.16
3	20×100	0.05	0.08
4	40×200	0.025	0.04
5	80×400	0.0125	0.02
6	160×800	0.00625	0.01
7	320×1600	0.003125	0.005

Table II. Co-ordinates of time-history points.

Points	X-co-ordinate	Y-co-ordinate
1	0.181	7.370
2	0.819	0.630
3	0.181	0.630
4	0.819	7.370
5	0.181	4.000

2.3. Physical data

A series of physical data are recorded at the following time-history points (Table II). Due to the staggered grids it is not always possible to get exactly the right value of the co-ordinates, so we choose the closest point.

The vorticity is defined as $\omega = \partial_x v - \partial_y u$, and the stream function ψ as $u = \partial_y \psi$ and $v = -\partial_x \psi$ with $\psi = 0$ on the walls. This last quantity is computed directly by integration from the walls.

To measure the skew symmetry of the temperature (see Reference [5]), the skewness is computed as

$$\varepsilon_{12} = \theta_1 + \theta_2 \quad (6)$$

where θ_1 and θ_2 denote the temperature at time-history points 1 and 2, this parameter should be zero for a skew-symmetric temperature field.

We define also

$$\Delta P_{ij} = P_i - P_j$$

where i and j indicate the time-history points.

The evaluation of Nusselt numbers are performed for each wall:

$$Nu(x=0, t) = \frac{1}{H} \int_0^H \partial_x \theta(0, y, t) dy, \quad Nu(x=L, t) = \frac{1}{H} \int_0^H \partial_x \theta(L, y, t) dy$$

In addition, the kinetic energy and the enstrophy provide useful metrics. That is

$$\|U\| = \sqrt{\frac{1}{2A} \int_A U \cdot U dA} \quad (\text{energy})$$

and

$$\|\omega\| = \sqrt{\frac{1}{2A} \int_A \omega^2 \, dA} \quad (\text{enstrophy})$$

where A is the area of the enclosure.

Finally, for all time-dependent computations, the average are computed, for a generic variable $\phi = u, v, \varepsilon, Nu, \|U\|, \|\omega\|$, as

$$\bar{\phi} = \frac{1}{T} \int_t^{t+T} \phi(x, y, t) \, dx \, dy$$

3. LINEAR STABILITY

3.1. Linear problem

We are interested in this section in the stability of the steady solution. In other terms, how far can a steady-state solution be observed physically? To answer this question we propose to compute the first Lyapunov exponent of the linearized system. We thus assume that a small perturbation (V, q, κ) is added to the steady solution (U_S, p_S, θ_S) of system (1). The stability study consists in looking at the behaviour of the perturbation along time. This behaviour is driven by the largest real part of the eigenvalues of the linearized problem. If the steady solution is stable, the perturbation goes to zero when t goes to infinity as $e^{\mu_1 t}$ where μ_1 is the first Lyapunov exponent. Thus, μ_1 is defined by using [8]:

$$\mu_1 = \lim_{t \rightarrow +\infty} \frac{\text{Log} \|(V(t), \kappa(t))\|}{t}$$

using the L^2 norm. Using the fact that (U_S, p_S, θ_S) is a steady-solution, we have to solve the simplified linear problem:

$$\begin{aligned} \partial_t V - \sqrt{\frac{Pr}{Ra}} \Delta V + \nabla q &= -U_S \cdot \nabla V - V \cdot \nabla U_S + \mathbf{e}_y \kappa && \text{in } \Omega \times (0, T) \\ \nabla \cdot V &= 0 && \text{in } \Omega \times (0, T) \\ \partial_t \kappa - \frac{1}{\sqrt{RaPr}} \Delta \kappa &= -U_S \cdot \nabla \kappa - V \cdot \nabla \theta_S && \text{in } \Omega \times (0, T) \\ V = V_0 \quad \text{and} \quad \kappa &= \kappa_0 && \text{in } \Omega \\ V &= 0 && \text{on } \partial\Omega \times (0, T) \\ \kappa &= 0 && \text{on } \Gamma_{\text{left}} \cup \Gamma_{\text{right}} \times (0, T) \\ \partial_y \kappa &= 0 && \text{on } \Gamma_{\text{bottom}} \cup \Gamma_{\text{top}} \times (0, T) \end{aligned} \tag{7}$$

where the non-linear terms $V \cdot \nabla V$ and $V \cdot \nabla \kappa$ are neglected.

3.2. Steady solution analysis

Problem (7) is solved exactly in the same way that the initial problem (1). The only difficulty is that the numerical solution (V^n, κ^n) at time $n\delta t$ becomes very small for large n . So, the solution is normalized at each time iteration by setting $(V_0^n, \kappa_0^n) = (V^n, \kappa^n) / \|(V^{n-1}, \kappa^{n-1})\|$ and the Lyapunov exponent is approximated by

$$\mu_1^n = \frac{\sum_{i=0}^{n-1} \text{Log} \|(V_0^i, \kappa_0^i)\|}{n\delta t}$$

if we take $\|(V_0, \kappa_0)\| = 1$. Here the Euclidean norm is used. For low Rayleigh numbers the convergence of the sequence μ_1^n is quite fast. But closer the Rayleigh number is to the critical Rayleigh number slower is the convergence of the sequence μ_1^n and longer must be the simulation time. In all cases the sequence $\|(V^n, \kappa^n)\|$ converges monotonically to zero and the sequence μ_1^n converges monotonically to μ_1 by lower values. To control the algorithm, we require that the norm of the solution (V^n, κ^n) is less than 10^{-10} . This is achieved rapidly for $Ra = 10^{+3}$ but is obtained for very large times T when the Rayleigh number is larger as shown in Table III.

On grid five 80×400 the steady solution is stable until $Ra \leq 2.5 \times 10^5$. At $Ra = 2.8 \times 10^5$ a slightly periodic solution has been found on this grid whereas on grid six 160×800 there is a stable steady solution (see Figure 3).

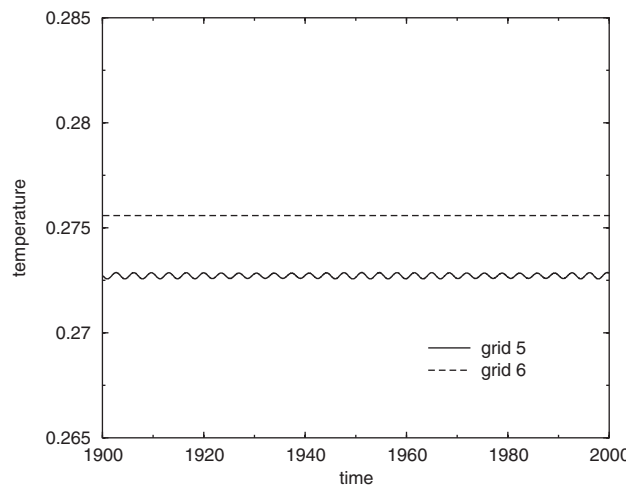


Figure 3. Temperature history at $Ra = 2.8 \times 10^5$ on the grid 5 at point $(0.18125, 7.37)$ and on the grid 6 at point $(0.178125, 7.375)$.

Table III. Evolution of the Lyapunov exponent, with Rayleigh number.

Ra	10^{+3}	10^{+4}	10^{+5}	$2 \times 10^{+5}$	$2.5 \times 10^{+5}$	$2.8 \times 10^{+5}$
T	60	185	453	623	915	3107
μ_1	-0.38	-0.12	-0.050	-0.036	-0.025	-0.008

Until $Ra=2.0 \times 10^5$ the computations of Lyapunov exponents are performed on grid five but for higher Rayleigh numbers the computations need a finer grid. A test for $Ra=2.5 \times 10^5$ shows that the value of μ_1 is the same on grids five and six. At $Ra=3.0 \times 10^5$ a slightly periodic skew-symmetric solution has been found on grid six which becomes more complex with a better resolution on grid seven 320×1600 as we shall see in the next section. These numerical tests suggest an estimate of the critical Rayleigh number between $Ra=2.8 \times 10^5$ and $Ra=3.0 \times 10^5$. A polynomial extrapolation of the curve obtained gives a value close to $Ra=2.9 \times 10^5$. We can see also in Table III that the Lyapunov exponent is very close to zero for such a value. Then, for Rayleigh numbers above the critical Rayleigh number stable unsteady solutions are captured. They are discussed in the next section.

4. NUMERICAL RESULTS FOR UNSTEADY SOLUTIONS

4.1. Results around the critical Rayleigh number

As we have seen in the previous section the solution is stationary until $Ra=2.8 \times 10^5$. We observe that the mean value of the temperature at the point 1 decreases when the Rayleigh number increases even for unsteady solutions (see in Figure 4). Computations on two consecutive grids show that the grid convergence is almost achieved as can be seen in Figure 4.

At $Ra=3.0 \times 10^5$ a non-skew-symmetric periodic solution is captured. Indeed, we can see in Figure 5 that the skewness is not zero on grid seven, it is a periodical function with a Fourier amplitude of 10^{-3} and a period of 3.7. In addition, the temperature history (Figure 5) and the phase portrait (Figure 6) show clearly the presence of two frequencies in the spectrum. Then, by increasing the Rayleigh number, a skew-symmetric periodic solution is found for a wide range of Rayleigh numbers.

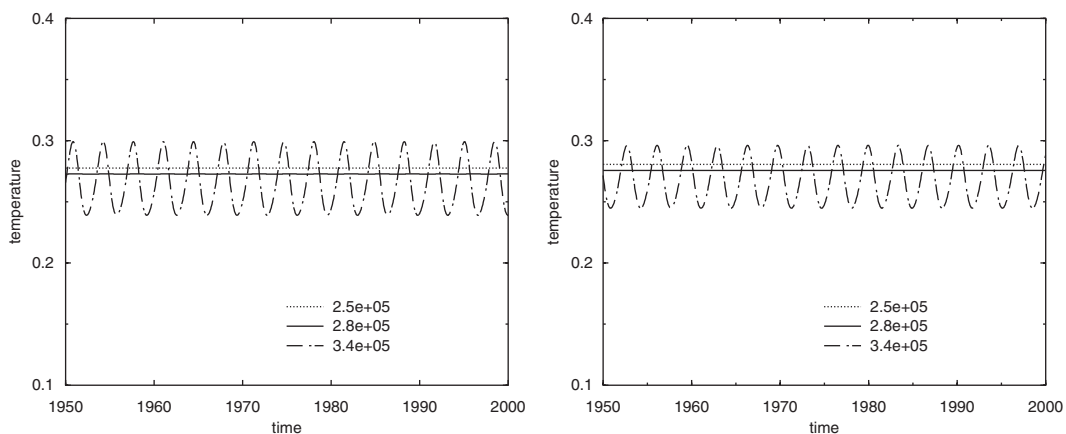


Figure 4. Temperature history for various Rayleigh numbers on grids 5 and 6 at the first point.

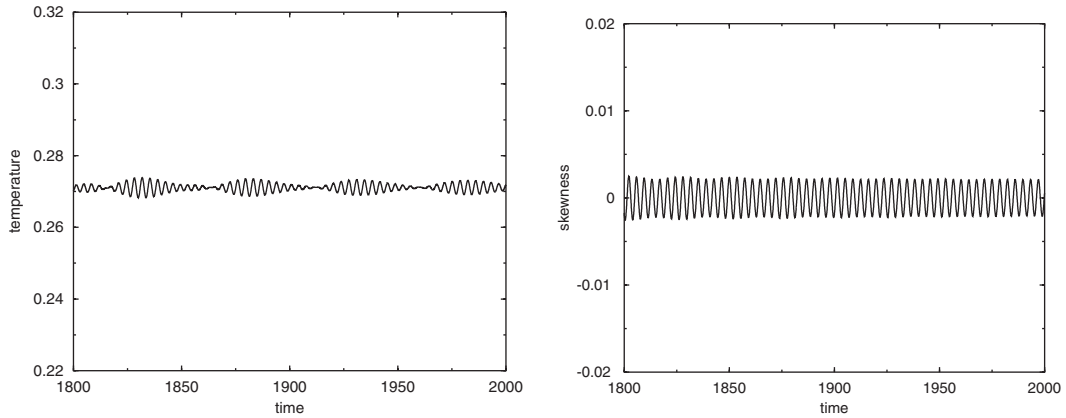


Figure 5. Temperature (left) and skewness (right) history at $Ra=3.0 \times 10^5$ on grid 7 at the first point.

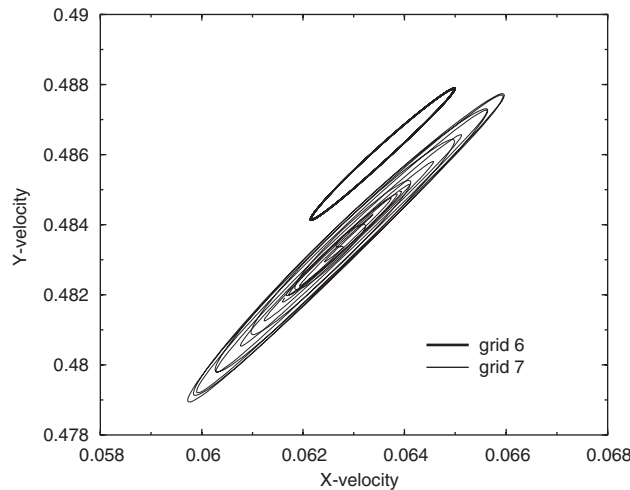


Figure 6. Phase portrait at $Ra=3.0 \times 10^5$ on grids 6 and 7 at the first point.

4.2. Results for $Ra=3.4 \times 10^5$

For comparison with the results presented in the special session at the first MIT conference, we propose to give some physical quantities at $Ra=3.4 \times 10^5$ which is a value for which the skew-symmetric periodic solution is well established. These results at $Ra=3.4 \times 10^5$ are listed below on four consecutive Cartesian grids of 40×200 , 80×400 , 160×800 and 320×1600 points in order to show the grid dependence. The time-history points used in this section correspond to the closest middle points of the staggered grid to the time-history points given in Table II. For instance the first point (0.181, 7.37) is replaced, respectively, by (0.1875, 7.38), (0.18125, 7.37), (0.178125, 7.375) and (0.179688, 7.3725) on the four grids. Unfortunately, the difference with the exact values induces some discrepancies in the results. We can see in Figure 7 that the mean value and the period for the temperature

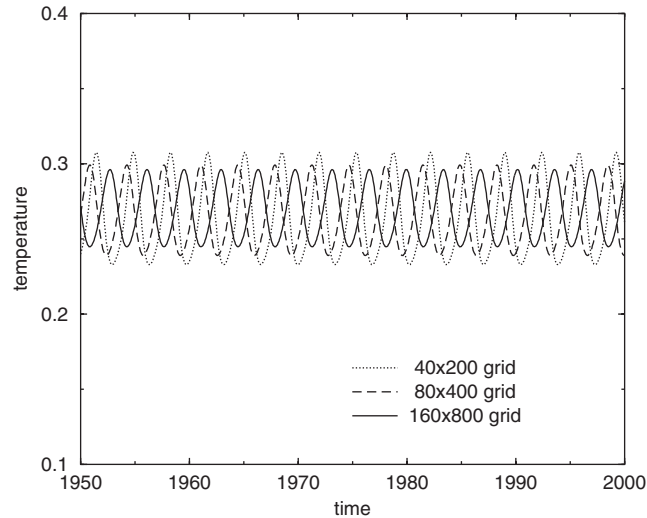


Figure 7. Temperature history for $Ra=3.4 \times 10^5$ on the 40×200 grid at point (0.1875, 7.38), on the 80×400 grid at point (0.18125, 7.37), on the 160×800 grid at point (0.178125, 7.375).

Quantity	Grid Resolution : 40×200 Time Duration : 2000 Steps per period : 300				Grid Resolution : 80×400 Time Duration : 2000 Steps per period : 600			
	Average	peak-to-val. amplitude	Fourier amplitude	Period	Average	peak-to-val. amplitude	Fourier amplitude	Period
X-Velocity	6.640e-2	1.016e-1	2.365e-2	3.4138	5.993e-2	7.811e-2	1.900e-2	3.4012
Y-Velocity	4.428e-1	1.134e-1	2.786e-2	3.4138	4.594e-1	1.022e-1	2.519e-2	3.4012
Temperature	2.645e-1	7.464e-2	1.809e-2	3.4138	2.661e-1	6.024e-2	1.482e-2	3.4012
Skewness	1.505e-5	2.120e-4	3.155e-5	3.4138	3.078e-6	6.390e-5	1.270e-5	3.4012
Stream func.	-5.960e-2	9.288e-3	2.134e-3	3.4138	-5.955e-2	7.895e-3	1.863e-3	3.4012
Vorticity	-1.946e+0	1.868e+0	3.784e-1	3.4138	-2.164e+0	1.583e+0	3.409e-1	3.4012
ΔP_{14}	-2.241e-3	3.158e-2	7.586e-3	3.4138	-1.795e-3	2.725e-2	6.620e-3	3.4012
ΔP_{51}	-5.440e-1	3.128e-2	7.707e-3	3.4138	-5.369e-1	2.908e-2	7.203e-3	3.4012
ΔP_{35}	5.462e-1	1.738e-2	4.353e-3	3.4138	5.386e-1	1.371e-2	3.444e-3	3.4012
Nusselt (θ)	-4.618e+0	1.183e-2	3.002e-3	3.4138	-4.585e+0	9.830e-3	2.455e-3	3.4012
Nusselt (W)	-4.618e+0	1.184e-2	3.005e-3	3.4138	-4.585e+0	9.830e-3	2.455e-3	3.4012
Energy	2.382e-1	5.100e-5	1.232e-5	3.4138	2.394e-1	4.200e-5	1.046e-5	3.4012
Enstrophy	2.394e+0	2.890e-3	7.261e-4	3.4138	2.702e+0	3.270e-3	8.186e-4	3.4012

Figure 8. Fourier analysis of time histories with 60 points per period at $Ra=3.4 \times 10^5$ on grids 4 and 5.

are different on the coarsest grid whereas the grid convergence is almost achieved on two finer grids. This can be seen also by looking at the results in Figures 8 and 9. The grid 320×1600 give the best results as in particular the skewness is very low but the convergence is almost achieved on the previous grid. So, the computations of the next section are performed on the grid 160×800 . We believe that this grid realize a good compromise between performance and accuracy and can give good qualitative behaviour of the solutions.

Quantity	Grid Resolution : 160 × 800 Time Duration : 2000 Steps per period : 1200				Grid Resolution : 320 × 1600 Time Duration : 200 Steps per period : 2400			
	Average	peak-to-val. amplitude	Fourier amplitude	Period	Average	peak-to-val. amplitude	Fourier amplitude	Period
X-Velocity	5.963e-2	6.617e-2	1.623e-2	3.4052	5.807e-2	6.075e-2	1.499e-2	3.4071
Y-Velocity	4.669e-1	8.881e-2	2.195e-2	3.4052	4.644e-1	8.359e-2	2.078e-2	3.4071
Temperature	2.685e-1	5.140e-2	1.273e-2	3.4052	2.668e-1	4.786e-2	1.177e-2	3.4071
Skewness	3.307e-7	8.770e-6	1.972e-6	3.4052	1.159e-7	4.327e-6	7.278e-7	3.4071
Stream func.	-5.857e-2	6.745e-3	1.615e-3	3.4052	-5.931e-2	6.256e-3	1.516e-3	3.4071
Vorticity	-2.218e+0	1.382e+0	3.140e-1	3.4052	-2.298e+0	1.233e+0	2.817e-1	3.4071
ΔP_{14}	-1.716e-3	2.377e-2	5.802e-3	3.4052	-1.787e-3	2.221e-2	5.469e-3	3.4071
ΔP_{51}	-5.377e-1	2.547e-2	6.294e-3	3.4052	-5.361e-1	2.408e-2	6.008e-3	3.4071
ΔP_{35}	5.394e-1	1.165e-2	2.925e-3	3.4052	5.379e-1	1.091e-2	2.748e-3	3.4071
Nusselt (0)	-4.580e+0	8.450e-3	2.110e-3	3.4052	-4.579e+0	7.820e-3	1.960e-3	3.4071
Nusselt (W)	-4.580e+0	8.450e-3	2.110e-3	3.4052	-4.579e+0	7.820e-3	1.960e-3	3.4071
Energy	2.396e-1	3.800e-5	9.447e-6	3.4052	2.395e-1	3.500e-5	8.856e-6	3.4071
Enstrophy	2.859e+0	3.300e-3	8.254e-4	3.4052	2.938e+0	3.270e-3	8.227e-4	3.4071

Figure 9. Fourier analysis of time histories with 60 points per period at $Ra = 3.4 \times 10^5$ on grids 6 and 7.

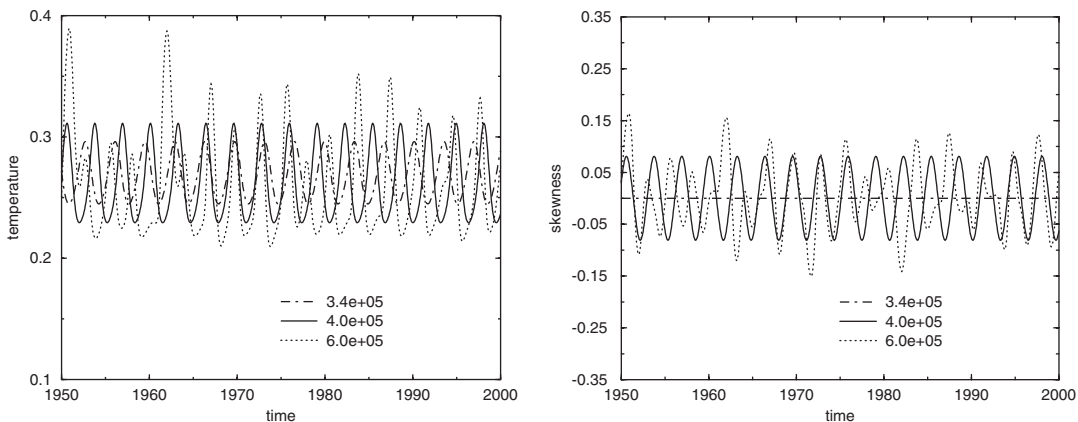


Figure 10. Temperature (left) and skewness (right) history for various Rayleigh numbers on grid 6 at the first point.

4.3. Results for higher Rayleigh numbers

Then, the solution is still a periodic one for Rayleigh number between 3.4×10^5 and 4.0×10^5 whatever the initial condition is (left-hand side of Figure 10).

This time the period decreases as the Rayleigh number increases. Moreover, the solution at $Ra = 4.0 \times 10^5$ is non-skew-symmetric as can be seen on the skewness history shown on the left-hand side of Figure 10. We observe that for the steady solution until $Ra = 2.8 \times 10^5$, the phase portrait is reduced to one point. Then for higher values of the Rayleigh number, in particular 3.4×10^5 and 4.0×10^5 the solution is purely periodic and the phase portrait for a long simulation time corresponding to 50 periods is a single closed curve. Whereas for a value

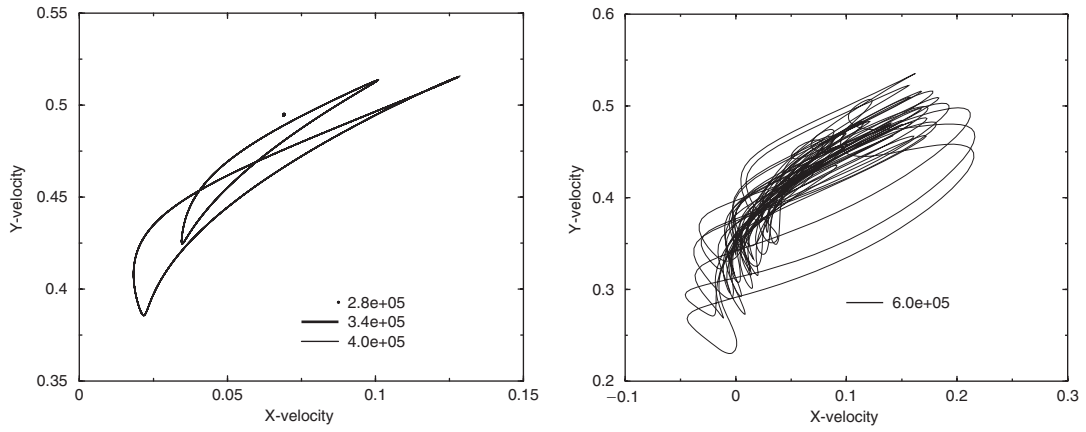
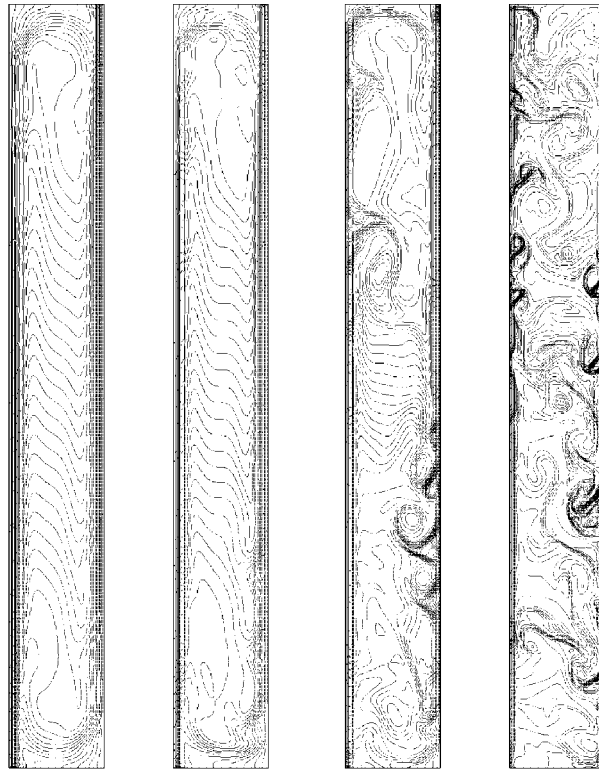


Figure 11. Phase portrait for various Rayleigh numbers on grid 6 at the first point.



3.4×10^5 6.0×10^5 3.0×10^6 3.0×10^7

Figure 12. Temperature isolines for increasing Rayleigh numbers at time 1000 on grid 6. The drawn isolines go from -2 to 2 by step 0.02 .

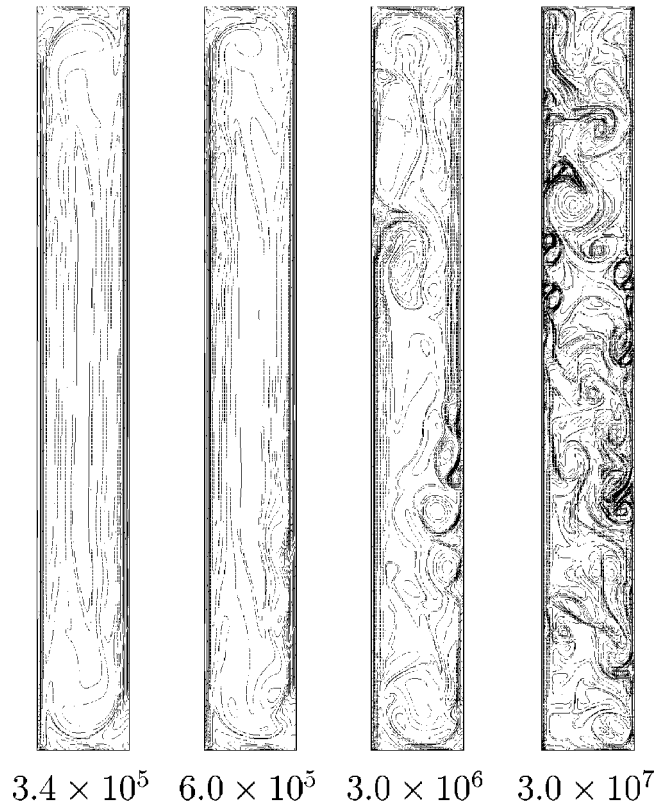


Figure 13. Vorticity isolines for increasing Rayleigh numbers at time 1000 on grid 6. The drawn isolines are: $-40, -30, -20, -15, -12, -10, -9, -8, -7, -6, -5, -4, -3, -2, -1, -0.1, 0.1, 1, 2, 3, 4, 5, 6, 7, 8, 9, 10, 12, 15, 20, 30, 40$.

just above as $Ra=6.0 \times 10^5$ the phase portrait indicates the presence of more frequencies in the spectrum (see Figure 11).

For higher values of the Rayleigh number, namely $Ra=3.0 \times 10^6$, and $Ra=3.0 \times 10^7$, a more complex solution is found. Indeed, we can see that the solution exhibits more and more activity along the vertical walls. This activity starts slightly at $Ra=6.0 \times 10^5$ to give a non periodic solution close to the periodic solution and then increases to give a chaotic solution at $Ra=3.0 \times 10^6$ and a fully developed turbulent solution at $Ra=3.0 \times 10^7$. The isolines of Figure 12 for the temperature and Figure 13 for the vorticity illustrate the increasing of vortex dynamics with the Rayleigh number. The vortices coming from the boundary layers are first confined in thin slices and then enter the whole domain as the Rayleigh number increases (see animation on the web site <http://www.math.u-bordeaux.fr/MAB/DNS>). In Figure 14, is plotted the average time enstrophy for various Rayleigh numbers. The value increases from the constant value 2.86 for the periodic solution to the mean values 2.99, 3.34 and 3.83 for the three other solutions. We can see in addition that the value is not constant anymore when the transition starts and that the amplitude increases with the Rayleigh number.

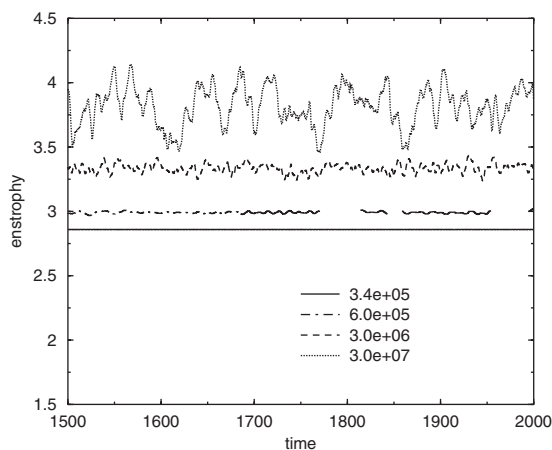


Figure 14. Evolution of average time enstrophy for various Rayleigh numbers on grid 6.

4.4. Computational resources

All the calculations of this paper have been performed on one processor of a Compaq ES40. The performances are given on the grid 80×400 .

- Clock rate 667 MHz
- Total memory 2000 MBytes
- specfp95 82.7
- CPU per grid point per time step $3.6 \mu\text{s}$
- Memory used 12 MBytes

5. CONCLUSIONS

The qualitative behaviour seems to be well captured by the multigrid method presented above. The main points of this approach are the explicit treatment of convection terms and their discretization by a third-order Murman scheme. The grid convergence is almost achieved on the 160×800 mesh where the computations are quite efficient. The proposed method allows to show that the solution can be stationary, skew-symmetric and periodic, non skew-symmetric and periodic, transitory, chaotic and even turbulent by increasing the Rayleigh number. An analysis of the linear stability, by the computation of Lyapunov exponent, allows to give an estimate of the critical Rayleigh number which seems to be quantitatively relevant.

REFERENCES

1. Fortin A, Jardak M, Gervais JJ, Pierre R. Localization of Hopf bifurcations in fluid flow problems. *International Journal for Numerical Methods in Fluids* 1997; **24**(11):1185–1210.
2. Fortin A, Jardak M, Gervais JJ, Pierre R. Old and new results on the two-dimensional Poiseuille flow. *Journal of Computational Physics* 1994; **115**(2):455–469.
3. Christon MA, Gresho PM, Sutton SM. Computational predictability of natural convection in enclosures. *International Journal for Numerical Methods in Fluids* 2002; **40**:953–980.

4. De Vahl Davis G, Jones IP. Natural convection in a square cavity: a comparison exercise. *International Journal for Numerical Methods in Fluids* 1983; **3**:227–248.
5. Le Quéré P, Behnia M. From onset of unsteadiness to chaos in a differentially heated square cavity. *Journal of Fluid Mechanics* 1998; **359**:81–107.
6. Bruneau Ch-H. *Numerical Simulation and Analysis of the Transition to Turbulence*, 15th ICNMF. Lecture Notes in Physics, vol. 490. Springer: Berlin, 1996; 1–13.
7. Bruneau Ch-H, Jouron C. An efficient scheme for solving steady incompressible Navier–Stokes equations. *Journal of Computational Physics* 1990; **89**(2):389–413.
8. Aston PJ, Dellnitz M. The computation of Lyapunov exponents via spatial integration with application to blowout bifurcations. Computational methods and bifurcation theory with applications. *Computational Methods in Applied Mechanics and Engineering* 1999; **170**(3–4):223–237.